引用格式：DU Yulin, XIE Xinrong, CHEN Hongsheng, et al. Hierarchical Spoof Plasmonic Structures Enhanced Terahertz Photoconductive Antenna (Invited)[J]. Acta Photonica Sinica, 2023, 52(10):1052410
杜遇林,谢欣荣,陈红胜,等.层级人工等离激元结构增强的太赫兹光电导天线(特邀)[J].光子学报,2023,52(10):1052410

层级人工等离激元结构增强的太赫兹光电导天线(特邀)

杜遇林[1,2],谢欣荣[1,2],陈红胜[1,2],高飞[1,2]
(1 浙江大学 杭州国际科创中心 极端光学技术与仪器全国重点实验室 量子信息交叉中心,杭州 310027)
(2 浙江大学 国际电磁科学院浙江大学分院 国际联合创新中心,海宁 314400)

摘 要:为提高太赫兹光电导天线输出效率,提出了一种基于层级人工等离激元结构的光电导天线的设计方法。层级人工等离激元结构由纳米尺度金属块阵列和微米尺度周期栅格结合而成,理论与仿真结果表明,前者通过人工局域表面等离激元谐振效应可提高光子-电子转换效率,后者则利用人工表面等离激元结构基模的禁带和高阶模式与电流源模式之间的正交性增强了光电导天线的垂直方向性。集成了层级人工等离激元结构的光电导天线结合了两种结构的优点,数值计算结果表明,其输出效率优于分别采用两种结构的方案。相较于未改进的光电导天线,层级人工等离激元结构在较宽频带范围内(0.86~1.51 THz)实现了光电导天线垂直方向辐射功率密度的提高。

关键词:光电导天线;太赫兹时域光谱技术;太赫兹源;人工表面等离激元;局域表面等离激元谐振
中图分类号:TN29 **文献标识码**:A **doi**:10.3788/gzxb20235210.1052410

0 Introduction

Terahertz (THz) waves have attracted extensive interest for their distinguished features in wave-matter interactions and have achieved two important applications, i.e., THz Time-Domain Spectroscopy (THz-TDS) and imaging technique[1-6]. However, the low output power of the THz radiation sources has put limitations on the signal-to-noise ratio and sensitivity of these two applications[7-8]. THz signals are mainly produced by optoelectronic means, and recently spintronic method has attracted great research efforts[9-10]. Photoconductive Antenna (PCA) is one of the most popular optoelectronic THz sources, and the typical pattern of which is a pair of electrodes deposited on a semiconductor substrate[11]. The general principle of PCAs is that femtosecond-laser-excited photocarriers are driven by a biasing voltages to generate picosecond pulse currents and emit THz waves. In such PCAs, the low-output issue is attributed to two aspects, i.e., the low photon-electron conversion efficiency, and low vertical directivity resulting from propagating Transmission Line (TL) modes along the horizontal electrodes.

To date, much effort has been devoted to addressing the low photon-electron conversion efficiency and low vertical directivity of PCAs, while being limited to solving these two problems separately. To improve the photon-electron conversion efficiency, two approaches have been proposed: adopting semiconductors with shorter carrier lifetime and higher carrier mobility[12-15] and integrating nanoscale plasmonic structures on the semiconductor[16-27]. Microscale metamaterial resonators have been integrated with PCAs to suppress the TL

Foundation item: The National Natural Science Foundation of China (Nos. 62171406, 11961141010, 61975176), the Key Research and Development Program of the Ministry of Science and Technology (Nos. 2022YFA1404902, 2022YFA1404704, 2022YFA1405200), the Zhejiang Provincial Natural Science Foundation (No. Z20F010018), the Key Research and Development Program of Zhejiang Province (No. 2022C01036), the Fundamental Research Funds for the Central Universities
First author: DU Yulin, duylin0328@zju.edu.cn
Contact author: XIE Xinrong, xinrongxie@zju.edu.cn; GAO Fei, gaofeizju@zju.edu.cn
Received: Jun.29,2023; **Accepted**: Sep.22,2023

electrode modes at specific frequencies, thus increasing the vertical directivities of PCAs in narrow bands[28-31]. WANG Chi et al. promoted this scheme by employing a microscale Spoof Surface Plasmon Polariton (SSPP) structure and realized broadband suppression[32]. However, the global output efficiency can only be increased sufficiently when the low photon-electron conversion efficiency and low vertical directivity are addressed simultaneously.

Here we propose hierarchical spoof plasmonic structures to increase the output efficiency of PCAs. Hierarchical structures combine nanoscale plasmonic structure and microscale SSPP[33-39] structure to address low-output issues from two aspects simultaneously. In detail, the metallic nanoblock array raises energy conversion efficiency by Spoof Localized Surface Plasmon Resonance (SLSPR), and periodic microscale gratings suppress horizontal radiation based on the forbidden band of the fundamental SSPP mode and the orthogonality between the electric dipole source and the higher-order SSPP mode. With the cooperation of hierarchical structures, the radiation power density in the vertical direction increases in a broad band from 0.86 THz to 1.51 THz.

1 Theory and simulation

Fig.1 shows the schematic diagrams of PCAs without and with hierarchical spoof plasmonic structures. Both PCAs adopt the Bottom-Located Thin-Film (BLTF) structure proposed by Burford N and El-Shenawee M [20], where golden electrodes are sandwiched between a Low-Temperature-grown Gallium Arsenide (LT-GaAs) substrate and a Si lens for shortening the carrier's average transport distance. The general principle of PCA follows that with an incident femtosecond laser beam, photocarriers are excited inside the semiconductor substrate, and the carrier population is propelled by biasing voltages applied on electrodes to form a picosecond current between central teeth pair, i.e., the anode and cathode (see Fig. 1). The photocurrent then generates $-z$-direction THz radiation converged by a Silicon (Si) collimating lens. Fig. 1(b) shows the hierarchical spoof plasmonic structures we proposed to address these two problems simultaneously, which includes a golden nanoblock array set above the substrate to elevate energy conversion efficiency and periodic teeth pairs integrated between electrodes along the x-axis to suppress horizontal radiation.

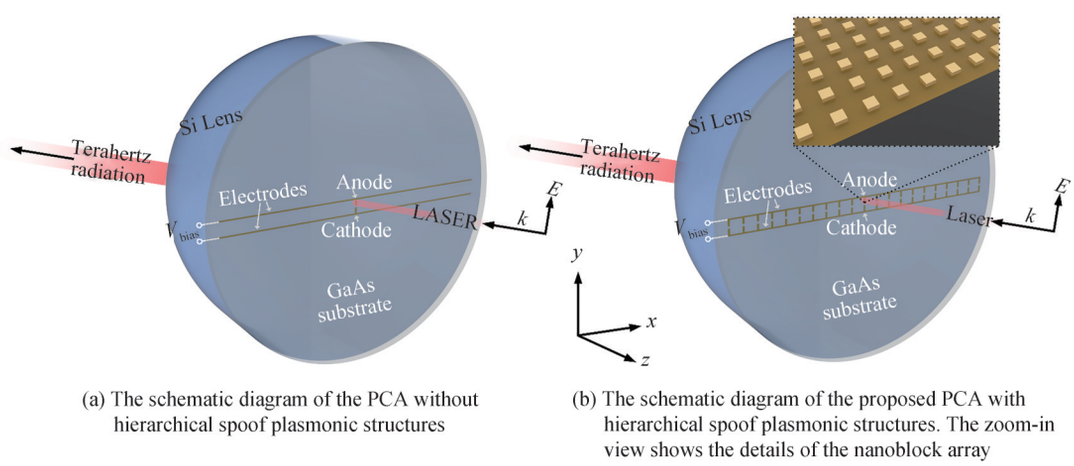

(a) The schematic diagram of the PCA without hierarchical spoof plasmonic structures

(b) The schematic diagram of the proposed PCA with hierarchical spoof plasmonic structures. The zoom-in view shows the details of the nanoblock array

Fig.1 The schematic diagrams of PCAs without and with hierarchical plasmonic structures. Both PCAs share a substrate-electrode-lens structure along the $-z$-direction

Firstly, we will analyze the influence of nanoscale plasmonic structure. Fig. 2(a) illustrates the anode-gap-cathode region, and the zoom-in view shows the details of the nanoblock array. The nanoblock with a square cross-section of $b\times b$, b=200 nm, and a thickness of t_1=75 nm, constructs a two-dimensional array with a center-to-center spacing of s=520 nm. Due to the nonlinear increase in the biasing electric field near the electrodes, it is beneficial for the electrodes to collect carriers when the laser is focused onto the gap asymmetrically. And as electrons mobility is significantly higher than that of holes, the laser which is focused onto the anode can further reduce average carrier transport path lengths[17]. The array is thus set only on the anode side according to the laser irradiation area. The laser is a Gaussian beam spatially, and a Gaussian pulse

temporally with a wavelength of $\lambda=800$ nm. Since the Fröhlich condition ($b<s<\lambda$) is satisfied, and the permittivity of gold ε_{Au} is negative according to the Drude model, SLSPR is excited under laser irradiation, leading to electric field enhancement around the structure, which corresponds to the conversion efficiency improvement. Here the nanoblock arrays can be treated as ensembles of interacting electric dipoles where the near-field coupling results in the suppression of scattering into the far field and the confinement of energy in the interstitial sites, presenting as resonant enhancement of the electric field.

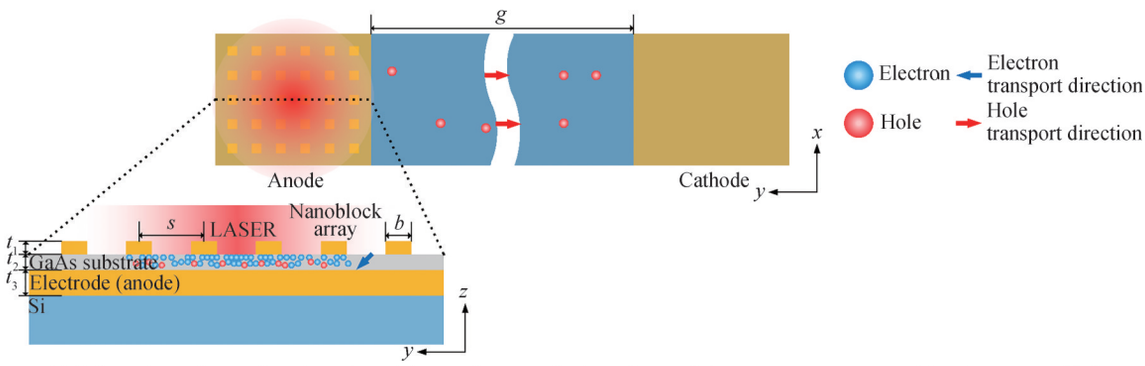

(a) Enlarged top view and section view of the anode-gap-cathode region, and the transport processes of the electrons and holes

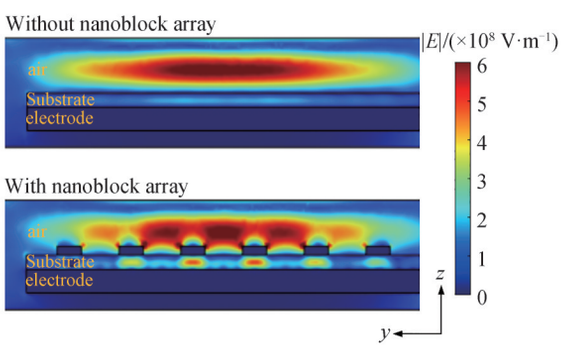

(b) The comparison of Electric field moduli on the *YZ*-section of the 3D COMSOL Multiphysics simulation models without and with nanoblock array

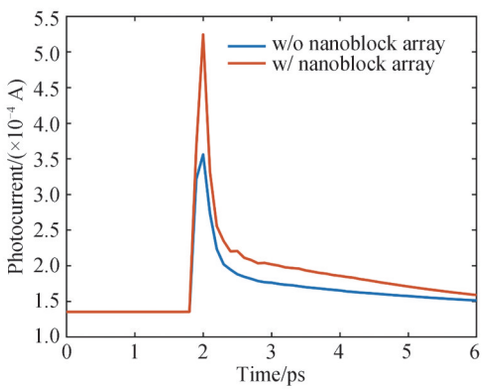

(c) The comparison of time-variant photocurrents without and with nanoblock array

Fig.2 The principle of improving conversion efficiency with nanoblock array

For quantitative analysis, we develop a three-dimensional simulation in COMSOL Multiphysics. The *y*-polarization laser beam is defined by [20]

$$E_y = E_0 \exp\left\{-2\ln(2)\times\left[\frac{(x-0)^2}{D_x^{\,2}}+\frac{(y-y_0)^2}{D_y^{\,2}}\right]\right\} \tag{1}$$

$D_x=D_y=2$ μm is Half Power Beam Width (HPBW), $(0, y_0)$ is the center point of the nanoblock array, and peak electric field E_0 is calculated by

$$E_0 = \sqrt{\frac{8\bar{P}\eta_0}{f_p D_x D_y D_t}}\left(-\frac{\ln 0.5}{\pi}\right)^{\frac{3}{4}} \tag{2}$$

where $\bar{P}=10$ mW is average power, $\eta_0=120\ \pi\Omega$ is free space wave impendence, $f_p=76$ MHz is pulse repetition rate, and $D_t=100$ fs is the Full Width at Half Maximum (FWHM). Laser parameters are also listed in Table 1. The nanoblock array scale is set to 5×6 to simplify the simulation. Since that only photocarriers generated within around 100 nm from the anode in LT-GaAs substrate will be collected due to the carrier's recombination effect, so we adopt a relatively thin LT-GaAs substrate with a thickness of $t_2=120$ nm to decrease the average transport distance to the anode of carriers and collect carriers as much as possible. Fig. 2(b) shows the electric field moduli on the *YZ*-section of the simulation models without and with the nanoblock array, respectively. Compared with the result without the nanoscale structure, a nanoblock array brings about significant electric

field enhancements at the edges of nanoblocks and inside the substrate under nanoblocks. Specifically, the volume average electric field amplitude of the substrate increases by about 1.52 times, from $7.317\ 4\times10^{7}$ V/m to $1.114\ 8\times10^{8}$ V/m, suggesting an elevation of energy transfer efficiency.

Table 1 Laser parameters

Symbol	Value & units	Description
λ	800 nm	Laser wavelength
D_x	2 μm	HPBW in the x-direction
D_y	2 μm	HPBW in the y-direction
D_t	100 fs	FWHM
t_0	2 ps	Pulse center location
$\bar{P}$	10 mW	Pulse average power
f_p	76 MHz	Pulse repetition rate
y_0	9.16 μm	y coordinate of the center point of the nanoblock array (also of laser)

Naturally, a stronger electric field will induce more photocarriers and generate a larger photocurrent. In COMSOL Multiphysics, we can use the electric field distribution results of the LT-GaAs substrate from the frequency domain study to calculate the transient photocarrier generation rate, which can be written as [20]

$$G=\frac{4\pi}{hc}k_{pc}\times P_{oav}\times\exp\left(-4\ln(2)\times\frac{(t-t_0)^2}{D_t^2}\right) \tag{3}$$

where h is Planck constant, c is the light speed in free space, $k_{pc}=0.086$ is the photoconductor extinction coefficient of LT-GaAs (i.e., the imaginary part of the refractive index of LT-GaAs), $t_0=2$ ps is the pulse center location, and the exponential term comes from temporal Gaussian property of laser as mentioned before. The time-average power flow of electric field P_{oav} establishes connections between the electromagnetic and semiconductor fields and is written as

$$P_{oav}=\sqrt{P_{oavx}^2+P_{oavy}^2+P_{oavz}^2} \tag{4}$$

Besides, we can get the electrostatic field distribution results from the stationary study (the applied biasing DC voltage is $V_{bias}=30$ V). The electrostatic field distribution results combined with the photocarrier generation rate enable us to get the terminal current between the anode and cathode (the gap distance is $g=10$ μm) by conducting a time-dependent study, in which the evolution process of carriers in LT-GaAs substrate is described by coupled Poisson's equation and drift-diffusion equation, and carriers recombination conforms Schottky-Read-Hall (SRH) recombination model and Auger recombination model. Related parameters of LT-GaAs are listed in Table 2. Simulation results are presented in Fig. 2(c) as the comparison of time-variant photocurrents. In both cases, photocurrents rise and fall drastically within 0.5 ps around 2 ps. With a nanoblock array, the peak value grows from $3.561\ 9\times10^{-4}$ A to $5.245\ 7\times10^{-4}$ A, and the increasing rate reaches around 47%, proving that the conversion efficiency has been increased. However, the horizontal radiation leakage is still to be solved to avoid its negative impact on global output efficiency.

The horizontal leakage is caused by TL modes propagating along the electrodes, which can be suppressed by optimizing the structure of the electrodes. Different from metamaterial resonator schemes[28-31], a broader bandwidth is attained from the bandgap of the SSPP structure. As Fig. 3(a) shows, the width of the electrode and tooth is $w=5$ μm and $a=5$ μm, respectively. The distances between the electrode pair are $d=40$ μm. Teeth are decorated periodically on both infinitely long electrodes, and the period length is $p=50$ μm. Periodic subwavelength gratings are a kind of classical spoof plasmonic structure that support the propagation of surface electromagnetic modes, but here it is used to restrict electromagnetic field from transversal propagating. We then conduct simulations using the eigenmode solver in CST Studio for further research. Fig. 3(b) and Fig. 3(c) are dispersion relations and electric field patterns of the unit cell circled by a dotted box in Fig. 3(a), respectively. The inset in Fig. 3(b) is the three-dimensional simulation model, where the thickness of electrodes is $t_3=200$ nm (see Fig. 2(b)), and the permittivity of LT-GaAs and Si are $\varepsilon_{GaAs}=12.9$ and $\varepsilon_{Si}=11.9$, respectively.

Table 2 LT-GaAs parameters

Symbol	Value & units	Description
n	3.57	The real part of the refractive index of LT-GaAs
k_{pc}	0.086	Photoconductor extinction coefficient
N_D	1×10^{15}/cm^3	Donor doping concentration
N_A	0	Acceptor doping concentration
E_g	1.424 V	Bandgap
χ	4.07 V	Electron affinity
μ_n	8 500 cm^2/(V·s)	Low-field electron mobility
μ_p	400 cm^2/(V·s)	Low-field hole mobility
τ_n	480×10^{-15} s	SRH electron lifetime
τ_p	480×10^{-15} s	SRH hole lifetime
C_n	7×10^{-42} m^6/s	Auger electron coefficient
C_p	7×10^{-42} m^6/s	Auger hole coefficient

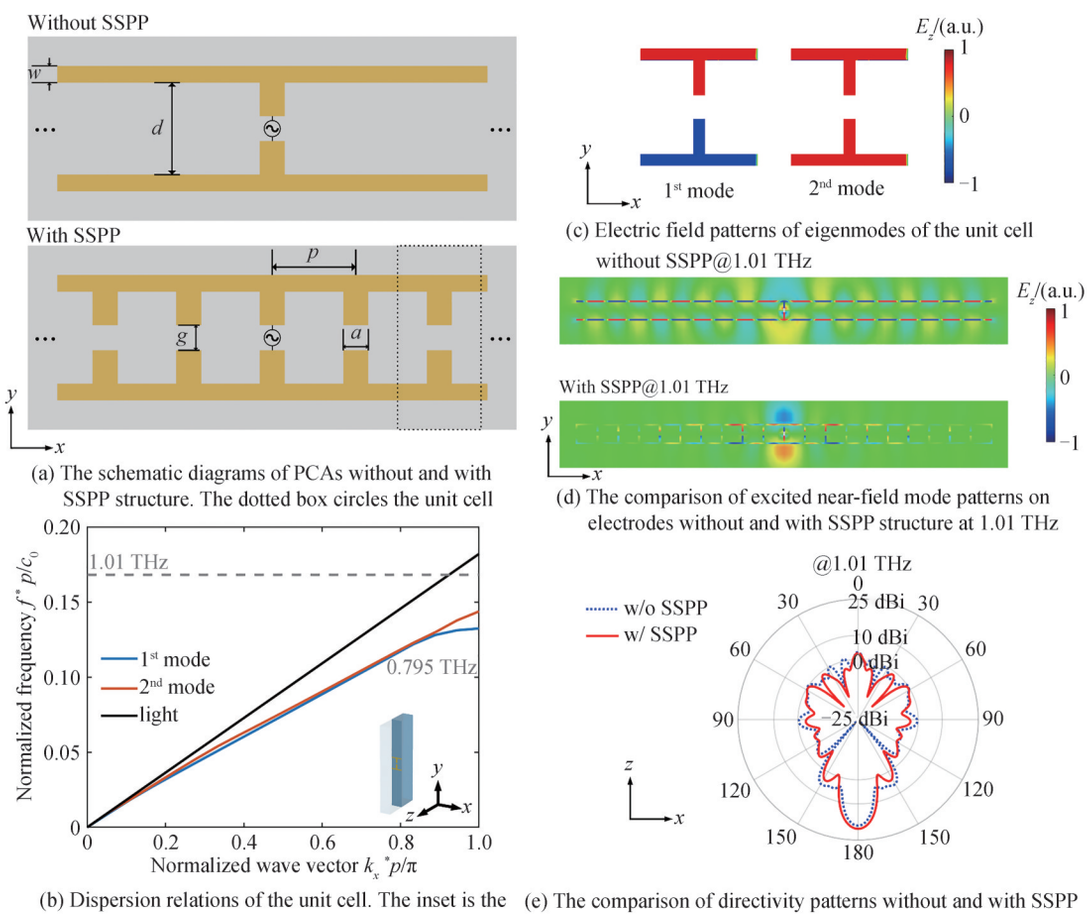

(a) The schematic diagrams of PCAs without and with SSPP structure. The dotted box circles the unit cell

(b) Dispersion relations of the unit cell. The inset is the 3D CST Studio simulation model

(c) Electric field patterns of eigenmodes of the unit cell without SSPP@1.01 THz

(d) The comparison of excited near-field mode patterns on electrodes without and with SSPP structure at 1.01 THz

(e) The comparison of directivity patterns without and with SSPP structure at 1.01 THz

Fig.3 The principle of improving vertical directivity with SSPP structure only

The boundaries along the x-direction are periodic boundaries, and along the y- and z- directions are electric boundaries. Observing Fig. 3(b), the two dispersion curves are lying below the light line, corresponding to two eigenmodes respectively. When the frequency is higher than the asymptomatic frequency (0.795 THz), the first eigenmode cannot be excited. Meanwhile, in terms of Fig. 3(c), the electric field pattern of the second eigenmode demonstrates y-even parity, which is orthogonal to the y-odd parity of the practical current source. Thus, the second eigenmode also cannot be excited efficiently even though the permissible band of higher-order eigenmode partially overlaps with the forbidden band of the first eigenmode. Both propagating modes arising

from the SSPP structure are unexcited as we expected, thus suppressing the horizontal radiation leakage in the operating frequency range.

Next, we conduct simulations by utilizing the time domain solver of CST Studio to validate the vertical directivity enhancement brought by the periodic gratings. The simulation model contains the whole antenna except for the nanoscale plasmonic structure. The radius and focus length of the Si collimating lens is r=550 μm and F=224.5 μm, respectively. All the geometry parameters of the microscale and nanoscale structures are listed in Table 3. And the electrodes with a finite length totally include 21 teeth. The practical photocurrent is replaced by a dipole source, representing a discrete constant unit current port connecting the anode and cathode, and lens focus coincides with it. Fig. 3(d) shows excited near-field mode patterns on electrodes at 1.01 THz without and with periodic gratings, respectively. It appears that the electromagnetic field propagates freely to the ends of bare electrodes, while on SSPP-modified electrodes, lateral propagation along the x-direction is almost blocked. The radiation power pattern shown in Fig. 3(e) provides a more intuitive result, from which we can see the horizontal directivity along the x-axis decreases by 3 dB, accompanied by the increase of the vertical directivity along the $-z$-direction from 19.00 dBi to 20.32 dBi.

Table 3 Structures geometry parameters

Symbol	Value & units	Description
b	200 nm	Side length of the nanoblock
s	520 nm	Center-to-center spacing of the nanoblock array
t_1	75 nm	Thickness of the nanoblock
t_2	120 nm	Thickness of the LT-GaAs substrate
t_3	200 nm	Thickness of the Au electrode
p	50 μm	Period length of the grating
a	5 μm	Width of the tooth
g	10 μm	Gap distance
d	40 μm	Distance between the electrode pair
w	5 μm	Width of the electrode
l	1 005 μm	Length of the electrode
r	550 μm	Radius of the Si lens
F	224.5 μm	Focus length of the Si lens

We further analyze the joint effect of the hierarchical structures composed of both nanoscale and microscale structures. The difficulty of trans-dimensional and multi-physical co-simulation denies the possibility of touching results directly with simulations, but a mathematical method can be adopted to connect the results of the nanoscale and microscale structures. The electrodes and lens compose a linear system where the output is the product of the input photocurrent and its spectral response and is proportional to the input photocurrent. Here the input photocurrents refer to the ordinary and nanoblock-enhanced photocurrents as we have discussed above, and they can be converted to the frequency domain using the Fourier transform. And the spectral responses of radiation power density in the $-z$-direction of the regular and SSPP-integrated antennas are obtained in CST simulations above, of which the excitation source is a constant amplitude current. By multiplying Fourier coefficients by corresponding frequency responses at the same frequency, we can achieve the vertical radiation power density spectra of PCAs under different circumstances (Fig. 4(a)). In the experiment, the reflection of THz wave at the Si-air interface because of the impedance mismatching will attenuate since material loss exists; while in the simulation, the material is lossless in ideal scenarios, and thus the resonance forming inside the Si lens will cause spectral oscillations, so here only the envelopes of THz signals are shown. The PCA with the hierarchical structure (red solid line) shows a huge increasement in vertical radiation power density compared with others in a broad band (0.86～1.51 THz, blue region) because it combines the advantages of both the nanoscale and microscale structures simultaneously. The necessity of these two structures is further analyzed. The comparison between the vertical radiation power density of the PCA with microscale structure only (orange dash-dotted line) and with hierarchical plasmonic structure (red solid line)

confirms that the introduction of nanoscale structure raises output efficiency over the whole simulation frequency range. On the other hand, the introduction of the microscale structure can be found to bring great improvement in downward radiation with a comparison between the vertical radiation power density of the PCA with the nanoscale structure only (green dotted line) and with hierarchical plasmonic structure. Here the working frequency range of the PCA with the microscale structure is 1.03～1.47 THz (green region), where the start frequency is slightly higher than the theoretical value because of the requirement of the sufficiently short evanescent length. The far-field power patterns shown in Fig. 4(b) further illustrate the functions of the microscale structure. We can see that the PCA with the nanoscale structure only owns the largest horizontal radiation since the increasement of the photon-electron conversion efficiency enlarges radiation power isotropically, but it's decreased with the introduction of the microscale structures to be even smaller than that with no structure (blue dashed line). Besides, it is surprising to find that in the $-z$-direction, the vertical radiation with microscale structure only is even stronger than that with the nanoscale structure only (see Fig. 4(b)). Quantitatively, at 1.27 THz, in the circumstance of the same input laser, radiation power density experiences a growth of 4.77 dB from -35.32 dBW/m^2 (2.94×10^{-4} W/m^2) to -30.55 dBW/m^2 (8.81×10^{-4} W/m^2).

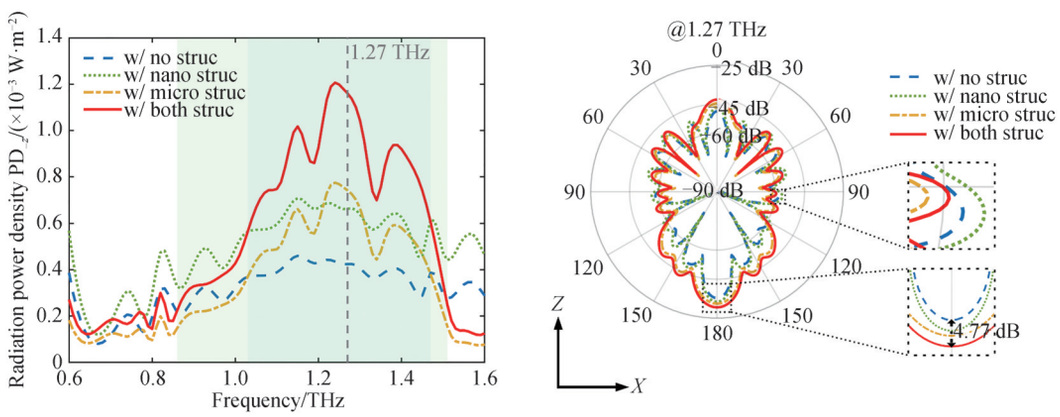

(a) The comparison of -z-direction radiation power density spectra of PCAs (only the envelopes of THz signals are shown)

(b) The comparison of far-field power patterns at 1.27 THz of PCAs (units: dBW/m^2). The zoom-in views show the details in the x and -z-directions

Fig.4 The comparison of output efficiencies of PCAs

Preparing for the experiments, the effects of the accuracies of the fabrication and operation are also studied. Regarding fabrication accuracy, for the metallic nanoblock array, localized surface plasmon resonance can be excited in arranged nanoscale metallic structures with arbitrary shapes under laser irradiation [40]. For the periodic microscale gratings, simulation results show that a simulated error of 100 nm for main geometry parameters affecting the start frequency of the forbidden band (i.e., the period length of the grating p, the width of the tooth a, the distance between the electrode pair d and the gap distance g, see Fig. 3(a)) causes a small fluctuation from -0.22% to 1.45%, indicating a negligible influence to the horizontal suppression. And concerning the experimental operation accuracy, for the typical PCA, the laser focus can only be at the edge of the anode at most because the metallic tooth is set above the semiconductor substrate; even if the laser is focused to a diffraction-limited spot size, the average electron transport path lengths are still relative long, only a minority of electrons can reach the anode in a sub-picosecond-scale time, while most remaining carriers will be recombined before being collected. In our work, however, profiting from the BLTF structure, photocarriers will generate when the laser focus is located inside the anode region. In other words, compared to the typical one, the PCA we proposed has a lower requirement for focus accuracy, and the spot size is unnecessary to down to the diffraction limit.

2 Conclusion

In this paper, hierarchical spoof plasmonic structures are introduced to improve the radiation power and

directivity of THz-PCA. The fundamentals are SLSPR enhancement of electric field and horizontal leakage suppression using the forbidden band of SSPP structure, respectively. We numerically demonstrate that the proposed PCA achieves higher output power density in a broad band from 0.86 THz to 1.51 THz. Using advanced micro/nano fabrication technology, PCA with hierarchical structures can be fabricated for further experimental measurement. With the explorations on semiconductor material engineering and the developments of higher efficiency THz collimating components, our proposal can enable more applications as a broadband THz source.

References

[1] COUTAZ J L, GARET F, WALLACE V P. Principles of terahertz time-domain spectroscopy[M]. Singapore: Pan Stanford Publishing, 2018.

[2] LU Xuyang, VENKATESH S, SAEIDI H. A review on applications of integrated terahertz systems[J]. China Communications, 2021, 18(5): 175-201.

[3] NEU J, SCHMUTTENMAER C A. Tutorial: an introduction to terahertz time domain spectroscopy (THz-TDS)[J]. Journal of Applied Physics, 2018, 124(23): 231101.

[4] ZUO Jian, ZHANG Liangliang, GONG Chen, et al. Research progress of super-continuum terahertz source based on nano-structures and terahertz lab on-chip system[J]. Acta Physica Sinica, 2016, 65(1): 010704.

[5] JIN Zuanming, PENG Yan, FANG Yuqing, et al. Photoinduced large polaron transport and dynamics in organic-inorganic hybrid lead halide perovskite with terahertz probes[J]. Light: Science & Applications, 2022, 11(1): 209.

[6] XU Guizhen, XING Hongyang, XUE Zhanqiang, et al. Recent advances and perspective of photonic bound states in the continuum[J]. Ultrafast Science, 2023, 3: 0033.

[7] VALUŠIS G, LISAUSKAS A, YUAN Hui, et al. Roadmap of terahertz imaging 2021[J]. Sensors, 2021, 21(12): 4092.

[8] ZHONG Kai, SHI Wei, XU Degang, et al. Optically pumped terahertz sources[J]. Science China Technological Sciences, 2017, 60(12): 1801-1818.

[9] ROUZEGAR R, CHEKHOV A L, BEHOVITS Y, et al. Broadband spintronic terahertz source with peak electric fields exceeding 1.5 MV/cm[J]. Physical Review Applied, 2023, 19(3): 034018.

[10] ISHIBASHI K, IIHAMA S, MIZUKAMI S. Different spin relaxation properties observed in linearly and circularly polarized laser induced terahertz emission from a Bi/Co bilayer[J]. Physical Review B, 2023, 107(14): 144413.

[11] SMITH P R, AUSTON D H, NUSS M C. Subpicosecond photoconducting dipole antennas[J]. IEEE Journal of Quantum Electronics, 1988, 24(2): 255-260.

[12] KROTKUS A. Semiconductors for terahertz photonics applications[J]. Journal of Physics D: Applied Physics, 2010, 43(27): 273001.

[13] DIETZ R J B, BRAHM A, VELAUTHAPILLAI A, et al. Low temperature grown photoconductive antennas for pulsed 1060 nm excitation: influence of excess energy on the electron relaxation[J]. Journal of Infrared, Millimeter, and Terahertz Waves, 2015, 36(1): 60-71.

[14] GLOBISCH B, DIETZ R J B, KOHLHAAS R B, et al. Fiber-coupled transceiver for terahertz reflection measurements with a 4.5 THz bandwidth[J]. Optics Letters, 2016, 41(22): 5262-5265.

[15] KOHLHAAS R B, BREUER S, LIEBERMEISTER L, et al. 637 μW emitted terahertz power from photoconductive antennas based on rhodium doped InGaAs[J]. Applied Physics Letters, 2020, 117(13): 131105.

[16] LEPESHOV S, GORODETSKY A, KRASNOK A, et al. Enhancement of terahertz photoconductive antenna operation by optical nanoantennas: Enhancement of terahertz photoconductive antenna operation by optical nanoantennas[J]. Laser & Photonics Reviews, 2017, 11(1): 1600199.

[17] BERRY C W, WANG Ning, HASHEMI M R, et al. Significant performance enhancement in photoconductive terahertz optoelectronics by incorporating plasmonic contact electrodes[J]. Nature Communications, 2013, 4(1): 1622.

[18] YANG Shanghua, HASHEMI M R, BERRY C W, et al. 7.5% optical-to-terahertz conversion efficiency offered by photoconductive emitters with three-dimensional plasmonic contact electrodes[J]. IEEE Transactions on Terahertz Science and Technology, 2014, 4(5): 575-581.

[19] WANG Ning, CAKMAKYAPAN S, LIN Y J, et al. Room-temperature heterodyne terahertz detection with quantum-level sensitivity[J]. Nature Astronomy, 2019, 3(11): 977-982.

[20] BURFORD N, EL-SHENAWEE M. Computational modeling of plasmonic thin-film terahertz photoconductive antennas[J]. Journal of the Optical Society of America B, 2016, 33(4): 748.

[21] BURFORD N M, EVANS M J, EL-SHENAWEE M O. Plasmonic nanodisk thin-film terahertz photoconductive antenna[J]. IEEE Transactions on Terahertz Science and Technology, 2018, 8(2): 237-247.

[22] PARK S G, JIN K H, YI M, et al. Enhancement of terahertz pulse emission by optical nanoantenna[J]. ACS Nano, 2012, 6(3): 2026-2031.

[23] HESHMAT B, PAHLEVANINEZHAD H, PANG Yuanjie, et al. Nanoplasmonic terahertz photoconductive switch on GaAs[J]. Nano Letters, 2012, 12(12): 6255-6259.
[24] SIDAY T, VABISHCHEVICH P P, HALE L, et al. Terahertz detection with perfectly-absorbing photoconductive metasurface[J]. Nano Letters, 2019, 19(5): 2888-2896.
[25] RANA G, BHATTACHARYA A, GUPTA A, et al. A polarization-resolved study of nanopatterned photoconductive antenna for enhanced terahertz emission[J]. IEEE Transactions on Terahertz Science and Technology, 2019, 9(2): 193-199.
[26] MITROFANOV O, SIDAY T, THOMPSON R J, et al. Efficient photoconductive terahertz detector with all-dielectric optical metasurface[J]. APL Photonics, 2018, 3(5): 051703.
[27] WANG Kemeng, GU Jianqiang, SHI Wenqiao, et al. All-dielectric nanograting for increasing terahertz radiation power of photoconductive antennas[J]. Optics Express, 2020, 28(13): 19144.
[28] SALAMIN Y, BENEA-CHELMUS I C, FEDORYSHYN Y, et al. Compact and ultra-efficient broadband plasmonic terahertz field detector[J]. Nature Communications, 2019, 10(1): 5550.
[29] DENG Hu, XIONG Zhonggang, QU Weiwei, et al. The impact of structural parameters of split-ring resonators on the terahertz radiation characteristics of micro-structured photoconductive antennas: a simulation study[J]. IEEE Photonics Journal, 2020, 12(3): 1-13.
[30] LEE K, LEE S C, KIM W T, et al. Terahertz generation by a resonant photoconductive antenna[J]. Current Optics and Photonics, 2020, 4(4): 373-379.
[31] SHI Xichen, WANG Kemeng, GU Jianqiang, et al. Photoconductive meta-antenna enabling terahertz amplitude spectrum manipulation[J]. Advanced Photonics Research, 2021, 2(1): 2000036.
[32] WANG Chi, ZHANG Zijian, ZHANG Youfei, et al. Enhancing directivity of terahertz photoconductive antennas using spoof surface plasmon structure[J]. New Journal of Physics, 2022, 24(7): 073046.
[33] GARCIA-VIDAL F J, FERNÁNDEZ-DOMÍNGUEZ A I, MARTIN-MORENO L, et al. Spoof surface plasmon photonics[J]. Reviews of Modern Physics, 2022, 94(2): 025004.
[34] ZHANG Xuanru, CUI Wenyi, LEI Yi, et al. Spoof localized surface plasmons for sensing applications[J]. Advanced Materials Technologies, 2021, 6(4): 2000863.
[35] GAO Zhen, WU Lin, GAO Fei, et al. Spoof plasmonics: from metamaterial concept to topological description[J]. Advanced Materials, 2018, 30(31): 1706683.
[36] PENDRY J B, MARTÍN-MORENO L, GARCIA-VIDAL F J. Mimicking surface plasmons with structured surfaces [J]. Science, 2004, 305(5685): 847-848.
[37] GAO Fei, GAO Zhen, LUO Yu, et al. Invisibility dips of near-field energy transport in a spoof plasmonic metadimer[J]. Advanced Functional Materials, 2016, 26(45): 8307-8312.
[38] YANG Yumeng, XIE Xinrong, LI Yuanzhen, et al. Radiative anti-parity-time plasmonics[J]. Nature Communications, 2022, 13(1): 7678.
[39] LI Yuanzhen, XU Su, ZHANG Zijian, et al. Polarization-orthogonal nondegenerate plasmonic higher-order topological states[J]. Physical Review Letters, 2023, 130(21): 213603.
[40] PARK S G, CHOI Y, OH Y J, et al. Terahertz photoconductive antenna with metal nanoislands[J]. Optics Express, 2012, 20(23): 25530.

Hierarchical Spoof Plasmonic Structures Enhanced Terahertz Photoconductive Antenna (Invited)

DU Yulin[1,2], XIE Xinrong[1,2], CHEN Hongsheng[1,2], GAO Fei[1,2]

(1 *Interdisciplinary Center for Quantum Information, State Key Laboratory of Extreme Photonics and Instrumentation, ZJU-Hangzhou Global Scientific and Technological Innovation Center, Zhejiang University, Hangzhou* 310027, *China*)

(2 *International Joint Innovation Center, the Electromagnetics Academy at Zhejiang University, Zhejiang University, Haining* 314400, *China*)

Abstract: Photoconductive Antenna (PCA) is the most common optoelectronic Terahertz (THz) source for the widely used THz Time-Domain Spectroscopy (THz-TDS) and imaging technique. But its application is still hindered by low output efficiency which originates from two issues, including low

photon-electron conversion efficiency, and low vertical directivity resulting from the horizontal leakage, i.e., propagating transmission line modes along the electrode pair of the PCA. However, current research can only achieve insufficient improvement in output efficiency since they are limited to solving the two issues separately. Here the hierarchical spoof plasmonic structures are proposed to enhance THz-PCA. Hierarchical structures combine the metallic nanoblock array and microscale Spoof Surface Plasmon Polariton (SSPP) periodic gratings together to solve the two issues simultaneously and increase the THz radiation output power. The PCA we proposed adopt a Bottom-Located Thin-Film (BLTF) structure where golden electrodes are sandwiched between a Low-Temperature-grown Gallium Arsenide (LT-GaAs) substrate and a Si lens, and the hierarchical structure includes a golden nanoblock array set above the substrate and periodic teeth pairs integrated between electrodes.

The improvement of conversion efficiency by nanoscale plasmonic structure is analyzed first. The nanoblock array is elaborately designed so that the Spoof Localized Surface Plasmon Resonance (SLSPR) is excited under laser irradiation, and leads to electric field enhancement around the structure. A three-dimensional multi-physical simulation is conducted using COMSOL. The simulation results show that a nanoblock array brings about significant electric field enhancements inside the substrate under nanoblocks compared to that without nanoscale structure. Specifically, the volume average electric field amplitude of the substrate increases by about 1.52 times. The photocurrent is simulated further and with a nanoblock array, the increasing rate of the peak value reaches around 47%.

Then the vertical directivity enhancement brought by the microscale SSPP structure is validated. When the frequency falls into the bandgap of the SSPP periodic gratings, the first-order SSPP mode is forbidden, and the second-order SSPP mode also cannot be excited efficiently due to the orthogonality between the dipole source pattern and the higher-order SSPP mode, thus suppressing the horizontal radiation leakage in the operating frequency range. Simulations conducted in CST Studio verify that the electromagnetic field propagates freely to the ends of bare electrodes (without SSPP periodic gratings), while on SSPP-modified electrodes, lateral propagation is almost blocked, and take the radiation power pattern at 1.01 THz as an example, the horizontal directivity decreases by 3 dB, accompanied by the increase of the vertical directivity.

Finally, the joint effect of hierarchical structures is investigated. As it is difficult to establish a trans-dimensional and multi-physical co-simulation, so a mathematical method is adopted to obtain the enhanced performance of the PCA with the hierarchical structures by connecting the results of the nanoscale and microscale structures. The electrodes and lens compose a linear system where the output is the product of the input photocurrent and its spectral response and is proportional to the input photocurrent. By multiplying Fourier coefficients of the ordinary and nanoblock-enhanced photocurrents by corresponding frequency responses of the regular and SSPP-integrated antennas at the same frequency, the vertical radiation power density spectra of PCAs under different circumstances are achieved. The PCA with the hierarchical plasmonic structures is better than those with two schemes separately, which shows a huge increasement in vertical radiation power density in a relatively broad operating band from 0.86 to 1.51 THz compared with the PCA without hierarchical structures. And the far-field power patterns quantitatively illustrate that at 1.27 THz, in the circumstance of the same input laser, radiation power density experiences a growth of 4.77 dB, confirming that hierarchical spoof plasmonic structures bring great improvements in the photon-electron conversion efficiency and vertical directivity of the THz-PCA.

Key words: Photoconductive antenna; Terahertz time-domain spectroscopy; Terahertz source; Spoof surface plasmon polariton; Localized surface plasmon resonance

OCIS Codes: 250.5403; 230.6080; 300.6495